Bulletin of the Seismological Society of America, Vol. 106, No. 4, pp. 1720–1732, August 2016, doi: 10.1785/0120150326

Joint Deconvolution of Building and Downhole Strong-Motion Recordings: Evidence for the Seismic Wavefield Being Radiated Back into the Shallow Geological Layers

by Bojana Petrovic and Stefano Parolai

Abstract In this study, the strong-motion recordings collected by a vertical array of borehole sensors and a network of accelerometers installed in a nearby building (distance between borehole and building ~10 m) are innovatively jointly analyzed through wavefield-deconvolution analysis. The analysis shows complicated patterns in the deconvolved wavefield of the borehole sensors that are interpreted by taking advantage of synthetic seismograms generated considering vertically propagating plane waves in the soil and building. Using a constrained deconvolution approach, we show that it is possible to separate the different components of the wavefield and, in particular, to retrieve the input ground motion and the wavefield radiated back by the building at different levels in the borehole, without *a priori* information about the attenuation structure (and velocity) of the building and soil. This therefore allows the energy radiated back by the structure at different depth to be estimated, which, in the case of the bottom of the borehole (at −145 m), is of the order of 10% of the energy of the input wavefield in the 1–10 Hz frequency band.

Introduction

In recent years, great attention has been paid to the seismic wavefield that is radiated back by a building in the free field, therefore modifying the amplitude of ground shaking during earthquakes (e.g., Bard *et al.*, 1996). Recent studies have focused on the multiple interactions between soil layers and civil engineering structures, the so-called "site–city interaction", by means of 2D and 3D numerical simulations of ground motion (e.g., Semblat *et al.*, 2002; Kahm *et al.*, 2006), concluding that the influence of site–city interaction can be significant. Empirical studies (e.g., Chavez-Garcia and Cardenas-Soto, 2002; Ditommaso *et al.*, 2010) have provided evidence of both soil–structure interaction and of the influence of a single vibrating building on the free-field ground motion. Since Snieder and Şafak (2006), several studies (e.g., Ditommaso *et al.*, 2009; Picozzi *et al.*, 2009; Newton and Snieder, 2012; Nakata *et al.*, 2013, 2015; Rahmani and Todorovska, 2013; Nakata and Snieder, 2014; Cheng *et al.*, 2015) have focused their attention on the study of wave propagation in buildings by using deconvolution interferometry. When coupled with standard engineering approaches such as modal analysis using frequency domain decomposition (Brincker *et al.*, 2001) or Fourier spectral analysis of an earthquake, active and/or passive source measurements, this approach allows the separation of the building's dynamic behavior from that arising from the soil–structure interaction. Deconvolution interferometry has also been extensively applied to borehole strong-motion data (e.g., Mehta *et al.*, 2007a,b; Parolai *et al.*, 2009, 2010; Oth *et al.*, 2011) to gain information about wave propagation in the shallow geological layers. However, a full picture of the wavefield propagation from the subsurface through the structure and back to it, and an identification and quantification of the wavefield radiated back from a structure to the soil, can only be obtained if simultaneous recordings from boreholes and instrumented buildings located nearby are available and jointly analyzed.

In 2011, the German Research Center for Geosciences (GFZ) installed a vertical array of six strong-motion sensors in a 150-m-deep borehole in the city of Bishkek, Kyrgyzstan (Parolai *et al.*, 2013) within the framework of cooperation with the Central Asia Institute for Applied Geosciences (CAIAG). The borehole is located in the courtyard of CAIAG and the nearby building of the institute is instrumented with seven Self-Organizing Seismic Early Warning Information Network (SOSEWIN; Fleming *et al.*, 2009) sensors located at different floors. The building is a three-story-reinforced masonry structure with a rectangular footprint. This 3D real-time sensor network has recorded four local earthquakes with magnitudes ranging between 4.8 and 5.2, which are particularly suitable for a comprehensive analysis of wave radiation by means of deconvolution interferometry.

In this study, the simultaneous recordings of earthquake data by the vertical array and building sensors are jointly

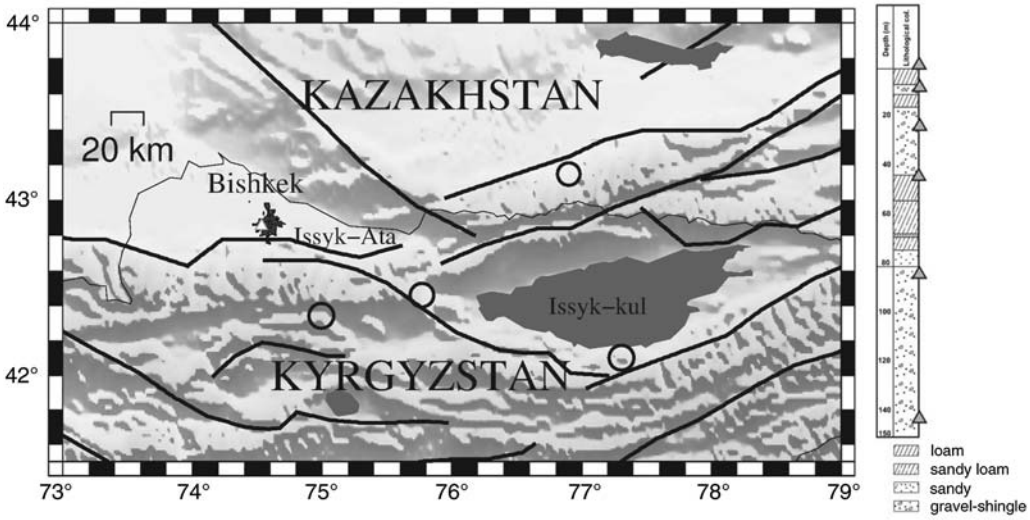

Figure 1. (left) Locations of the epicenters (circles) of earthquakes used in this study and listed in Table 1, and (right) the Bishkek vertical array stratigraphic column. The triangles on the stratigraphic column mark the depths of the borehole instruments. The black lines show the known faults in this area.

analyzed by deconvolution interferometry to estimate the Green's functions related to the wave propagation in the borehole, through the building and back. In this way, an overall picture of the wave propagation is obtained and the wavefield that is radiated back from a structure to the soil at different depths is investigated and isolated. To interpret the deconvolution interferometry results, numerical simulations of ground motions are carried out, considering the building structure to be described as a simple shear beam (Iwan, 1997). The synthetic seismograms calculated are then deconvolved in the same way as the real data. The results are compared with those obtained from the real data and discussed. Finally, and innovatively, the proportion of the seismic wavefield that is radiated back by the structure into the shallow geological layers is estimated by, (1) the real input ground motion (after downgoing waves reflected at the surface and discontinuities between different soil layers and at the top of the building are removed) at the bottom seismometer and at 10 m depth is estimated and (2) the ground motion relevant only to the downgoing waves radiated back by the building is extracted from the recorded seismograms using an approach similar to the constrained deconvolution proposed by Bindi *et al.* (2010).

Array Description

A 150-m-deep borehole was drilled in the courtyard of CAIAG in Bishkek (Fig. 1). The borehole is equipped with a three-component accelerometer at the surface, and a chain of five three-component borehole accelerometers at depths of 10, 25, 45, 85, and 145 m. The sensors are connected to two 24-bit digitizers. The output is set to $\pm 2g$ and the sampling rate is 500 samples per second. The orientation of the sensor components with respect to the cardinal points was obtained by low-pass filtering the seismograms at 1 Hz (i.e., below the frequency affected by downgoing waves, following Parolai *et al.*, 2013) and rotating the recordings of each sensor with respect to the recordings at the surface by steps of 1°. For each rotation angle, the cross correlations are calculated and the recorded components are rotated in the direction leading to the maximal cross correlation. Finally, the borehole sensors are oriented along the main building axes. The borehole, cased along its entire length, crossed several quaternary layers (Parolai *et al.*, 2010, and references therein). In particular, the uppermost 80 m are dominated by alternating layers of coarse gravel shingle and sandy layers with varying thicknesses (Fig. 1), whereas below 80 m depth only one thick gravel-shingle layer is present until the final depth. The groundwater table was encountered at a depth of 55 m. Using the deconvolution interferometry of only one event recorded by a few borehole instruments, Parolai *et al.* (2013) estimated that the *S*-wave velocity in the shallowest 15 m is 500 m/s, increasing to 700 m/s by a depth of 43 m, at which it increases to 820 m/s until 75 m. Between 75 m depth and the bottom of the borehole, an *S*-wave velocity of 1590 m/s was estimated. These values are also in fair agreement with the *S*-wave velocity estimated by Rayleigh-wave dispersion curve inversion (Parolai *et al.*, 2010). The quality factor for *S* waves Q_S was estimated to be around 5 for the shallowest 15 m and around 50 for the remaining investigated depth.

The CAIAG building (Fig. 2) is a three-story-reinforced masonry structure with a rectangular shape, 37.81 m long and 16.3 m wide and was built in 1975. The walls are made of fired clay solid bricks and the lateral resistance is provided by the walls themselves. The floor is made of concrete and the floor system type can be described as a pre-cast concrete floor with reinforced concrete topping. The roof is pitched and hipped and made of wood covered by metal or asbestos. Six SOSEWIN units (Fleming *et al.*, 2009; Bindi *et al.*, 2015) are installed at the two edges of the three floors of

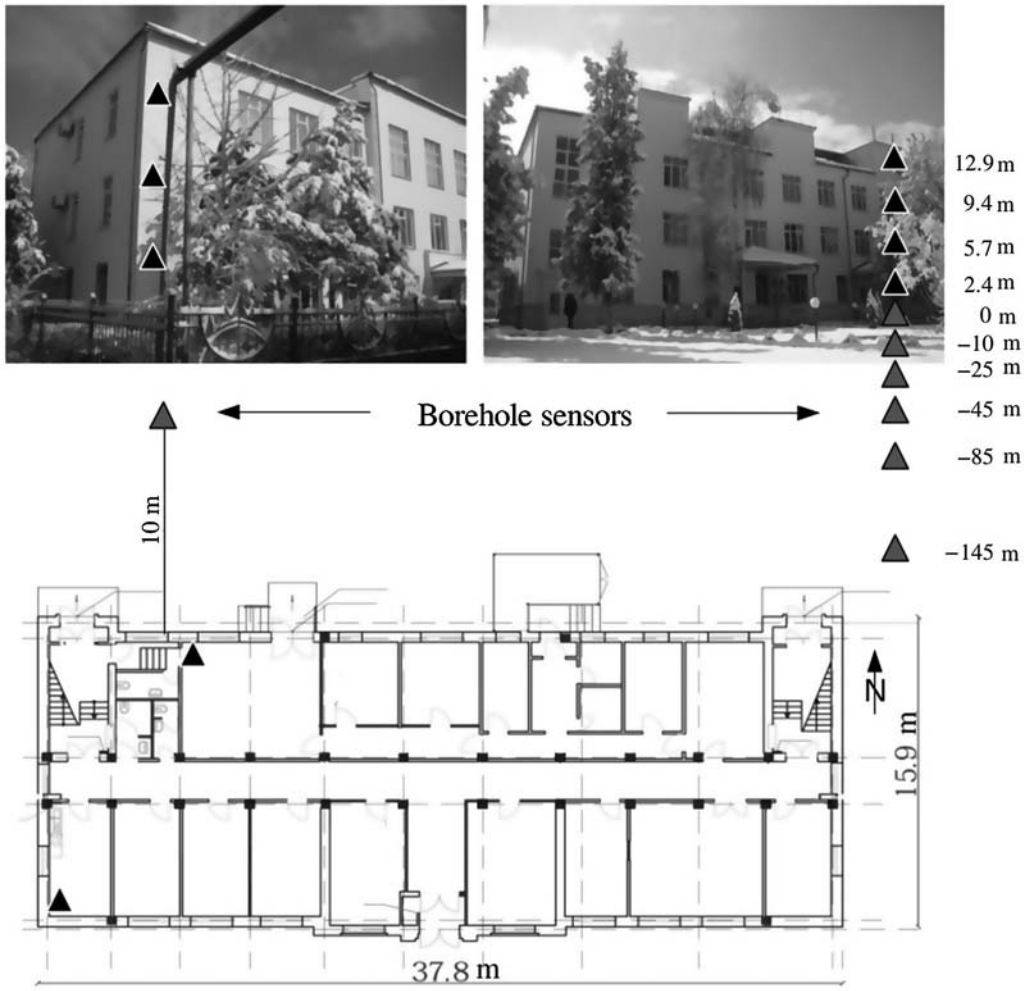

Figure 2. Self-Organizing Seismic Early Warning Information Network (SOSEWIN) installations in the Central Asia Institute for Applied Geosciences (CAIAG) building (black triangles) and borehole sensors (gray triangles). Top left panel, view from south; top right panel, view from north; bottom panel, footprint.

the building, with one unit installed under the roof. These units are equipped with a microelectromechanical systems sensor with a sampling rate of 100 samples per second. A detailed description of these units is provided by Fleming *et al.* (2009). The data are stored locally and transmitted in real time via the Internet to CAIAG and the GFZ.

Methodology

The deconvolution of ground motion recorded at a depth $z1$ with that at depth $z2$ can be written in the frequency domain as

$$S(\omega) = \frac{u(z1,\omega)}{u(z2,\omega)}, \tag{1}$$

in which $u(z1,\omega)$ and $u(z2,\omega)$ are the Fourier transforms of the motions recorded at depths $z1$ and $z2$, respectively. However, the deconvolution operation is applied to data corrupted by noise and, therefore, this problem is ill-conditioned because small errors in the data could lead to solutions that are unacceptable from a physical point of view.

To avoid this instability, a regularized Tikhonov deconvolution $S_\varepsilon(\omega)$ is used (Tikhonov and Arsenin, 1977; Bertero and Boccacci, 1998; Mehta *et al.*, 2007a,b; Parolai *et al.*, 2009):

$$S_\varepsilon(\omega) = W_\varepsilon(\omega)\frac{u(z1,\omega)}{u(z2,\omega)}, \tag{2}$$

in which $u(z1,\omega)$ and $u(z2,\omega)$ denote the Fourier spectra of the deconvolved wavefield and

$$W_\varepsilon(\omega) = \frac{|u(z2,\omega)|^2}{|u(z2,\omega)|^2 + \varepsilon} \tag{3}$$

is the filter. ε is the regularization parameter and refers to a constant added to the denominator to prevent the numerical instability of equation (1).

Consistent with the results of Mehta *et al.* (2007a,b) and Parolai *et al.* (2009) who showed the independence of the deconvolution results of the signal window used, but with their dependence on the analyzed component of ground acceleration, no window selection was carried out. In this way,

Table 1
List of Events used in This Study

ID	Origin Time (yyyy/mm/dd hh:mm:ss) (UTC)	Magnitude (M_w)	Latitude (°)	Longitude (°)	Depth (km)
1	2013/11/23 09:42:07	4.9	42.526	75.711	9.8
2	2014/11/14 01:24:15	5.2	42.093	77.262	10.0
3	2015/01/22 15:52:30	4.9	42.362	74.951	21.3
4	2015/03/15 14:01:03	4.8	43.073	76.911	27.9

the results obtained by deconvolving the horizontal component of ground motion are expected to be related mainly to the *S*-wave propagation function.

Data

In this study, the recordings of four earthquakes with magnitudes ranging between 4.8 and 5.2 (Fig. 1 and Table 1) that occurred in Kyrgyzstan and Kazakhstan between 2013 and 2015 are analyzed. Because of small ground motion of the analyzed earthquakes, linear behavior can be assumed.

Figure 3 shows, as an example, the north–south component of recordings of event ID 4 (Table 1), corresponding to the transverse direction of the building. The modification of ground motion at different depths is obvious, as well as the larger level of shaking observable at the top of the building (note in the figure the different scales used for plotting the borehole and building data). The Fourier spectra amplitudes of the recordings also show the frequency dependence of the ground-motion variability at different depths and a clear resonant peak (likely corresponding to the first mode of the structure at around 5 Hz). Because of the different quality of the instruments used, the signal-to-noise ratio is higher in the borehole recordings. The data collected in the building have been reinterpolated to 500 samples per second to harmonize them with those collected by the borehole array, before calculating the Fourier transform.

Results

Joint Deconvolution

The existence of peaks in the acausal and causal part of the deconvolved wavefields that can be related to upward and downward propagating waves is obvious from Figure 3. The spectra of the deconvolved wavefields show spectral troughs at frequencies affected by the downward-going waves that can be directly related to the travel times of the *S* waves in the building-soil structure and therefore to their velocities in each layer. Interestingly, the trough at 0 m depth occurs at nearly 5 Hz (consistent with the resonant peak of the building, which is likely to correspond to the first translational [and dominant] mode of the structure), whereas the first spectral trough in the deepest sensor (145 m) occurs at around 2 Hz. The spectrum of the deconvolved wavefield at the reference station (station at the roof) is flat until 15 Hz, where it starts to decrease, therefore indicating where the influence of the filter $W_\varepsilon(\omega)$ is strongest.

Figure 4 shows the deconvolved wavefield obtained for the transverse direction of ground motion for all the events listed in Table 1 (left) and the results obtained after stacking (right). In the acausal part of the deconvolved wavefield results for the downhole seismometer, a clear upward propagating pulse can be identified (first black line). When the pulse reaches the Earth's surface, a part of the energy is reflected back into the soil, as is clearly visible from the downward-going wave pulse that can be followed until the deepest sensor (black dashed-dotted line). The remaining part of the wavefield is transmitted into the building and propagates until its top (first black line), where it is reflected back (black-dashed line). When reaching the Earth's surface again, the waves are transmitted into the ground (with a pulse that is then visible until the deepest sensor) and, although less clearly visible, reflected back (due to the impedance contrast between the building with lower velocity and the soil material with higher velocity) with a change of polarity in the building. We will show later that two peaks belonging to different pulses overlie each other (see also Appendix). As a matter of fact, the same black-dashed line marks two different pulses. The velocity inside the building can be estimated from the arrival times of the pulses at different floors, and is found to be around 300 m/s.

Differing from the cases of wave propagation in nearly homogeneous materials, for example, in Parolai *et al.* (2009), the acausal part of the signal is not dominated by a single peak but by a couple of them (indicated by the black lines from −145 to 0 m depth) moving in parallel along the time axes.

To better understand the wave propagation within the soil-building structure, numerical simulations were carried out using the Wang (1999) approach (and used in the forward propagation part of the inversion code employed by Parolai *et al.*, 2012, 2013). The building structure was simulated by considering a shear-beam approximation and therefore by adding a layer with an *S*-wave velocity of 300 m/s, a density of $\rho = 400$ kg/m^3, appropriated for this kind of reinforced masonry structure, and a Q_S of 10 (equivalent to a 5% damping), at the top of the soil structure. Although simple, it has been shown that this model can capture the main features observed in real data (far source) analyses. The *S*-wave velocity and Q_S profiles used were taken from the best ones calculated by Parolai *et al.* (2013). Figure 5 shows the propagation of *S* waves with nearly vertical incidence between the deepest borehole sensor and the top of the building.

Consistent with Parolai *et al.* (2013), part of the energy of the upward-going *S* wave, when reaching the 75-m depth

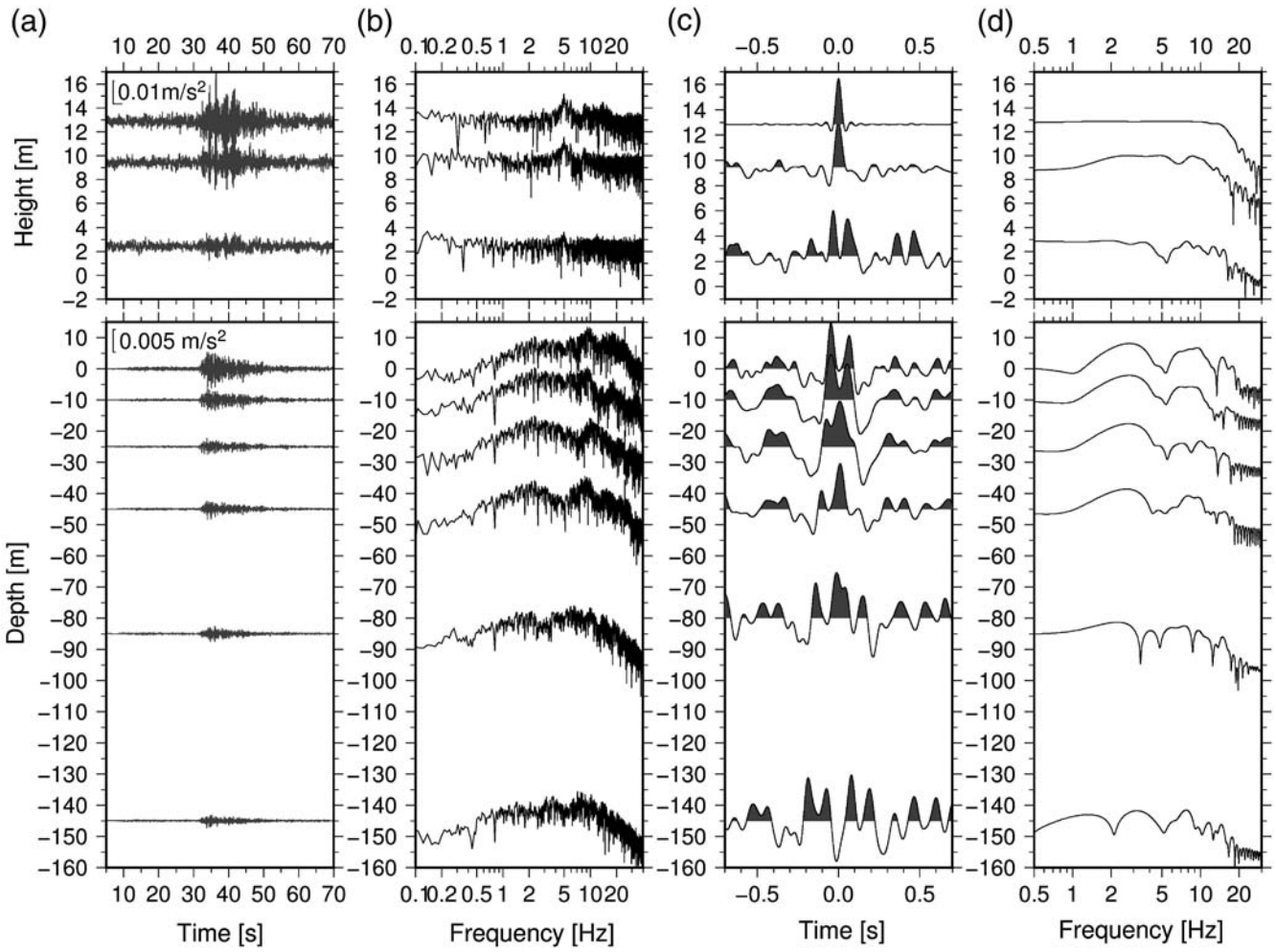

Figure 3. (a) North–south component (corresponding to the transverse direction of the building) recordings of the borehole accelerometers (from −145 to 0 m) and the SOSEWIN sensors (2–13 m) of the M_w 4.8 event that occurred on 15 March 2015 (ID 4, Table 1). Please note the two different scales used for the plots, differing in a factor of 2. (b) Fourier amplitude spectra of the recordings, (c) deconvoled wavefield using the recording at the top of the building as reference, and (d) the spectra of the deconvolved wavefields.

discontinuity between the loam and the gravel shingle, is reflected back. The energy transmitted through the discontinuity is propagated toward the surface where the first downward-going wave is generated. The transmitted energy inside the building propagates as an upward-going wave and reaches the top of the structure where a second downward-going wave is generated. When reaching the Earth's surface, the downward-going wave is both reflected back to the top of the structure (with a change of polarity) and transmitted down through the Earth.

Figure 6 shows the deconvolved wavefield results obtained using the synthetic seismograms (gray) and the observed data (black). The high level of similarity between the two results is clearly visible, although, probably due to the usage of a narrower frequency bandwidth for the analysis of the observed data (f = 1–10 Hz) due to the signal-to-noise ratio, the real data show a worse separation of the single peaks. In any case, although the velocity of propagation of the S waves in the deepest part of the adopted model for the synthetic seismogram seems to be slightly too low (note the slight mismatch in the observed and calculated downward-going peaks), the favorable comparison between the observed and synthetic deconvolved wavefields allows us to assign univocally each of the observed peaks to a particular up and downward-going phase and to update the velocity model.

Estimation of the Wavefield Radiated Back to the Soil

The first step in this section involves the more detailed interpretation of the peaks obtained from the deconvolution of the observed signals using the analytical transfer functions derived for two- and three-layer building-soil structure (see the Appendix for their derivation). When considering the soil layer (and the sensors) above 75 m depth (two-layer model), the double peak dominating the acausal part of the signal (Fig. 6, black lines) can be explained by considering the first one to be related to the upward-going propagation of the wavefield (equation A4a), whereas the second (equation A4c)

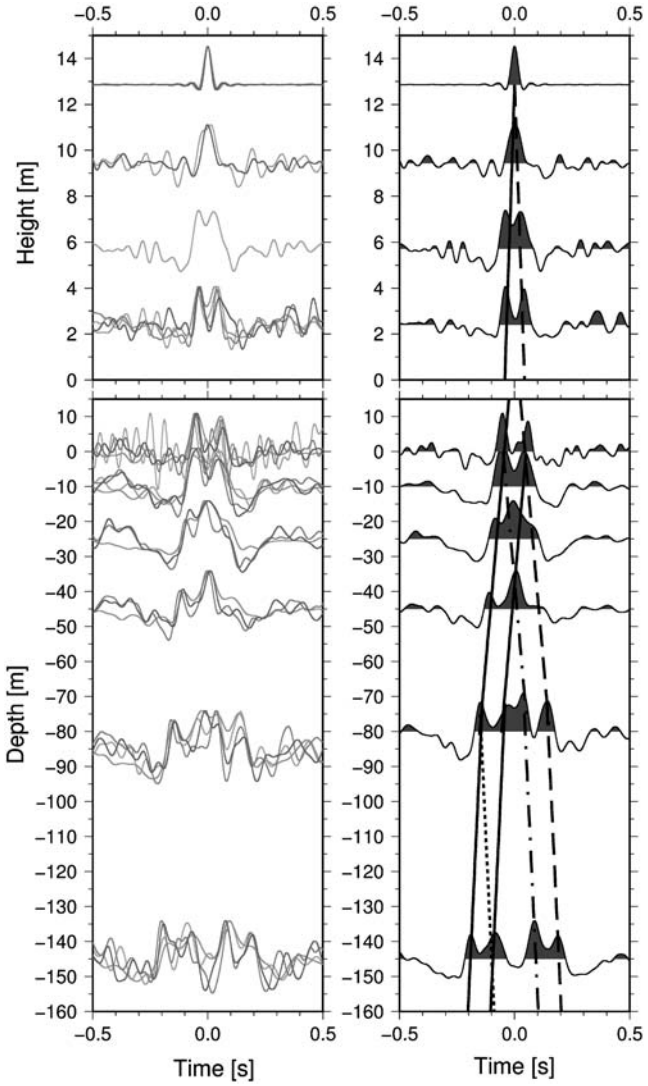

Figure 4. (Left panel) Deconvolved wavefields obtained for the north–south component of ground motion arising from the four considered events (Table 1) using the recordings from the top of the building as the reference. There is only one line at 6 m, because the sensor at the 2nd floor had some problems and hence, registered only one of the four analyzed earthquakes. (Right panel) The results obtained after stacking the results shown in the left panel. The upward-going waves (black lines), the downward-going waves reflected at the interface at 75 m depth (black-dotted line), at the Earth's surface (black dashed-dotted line) and at the top of the building (dashed line) are also shown.

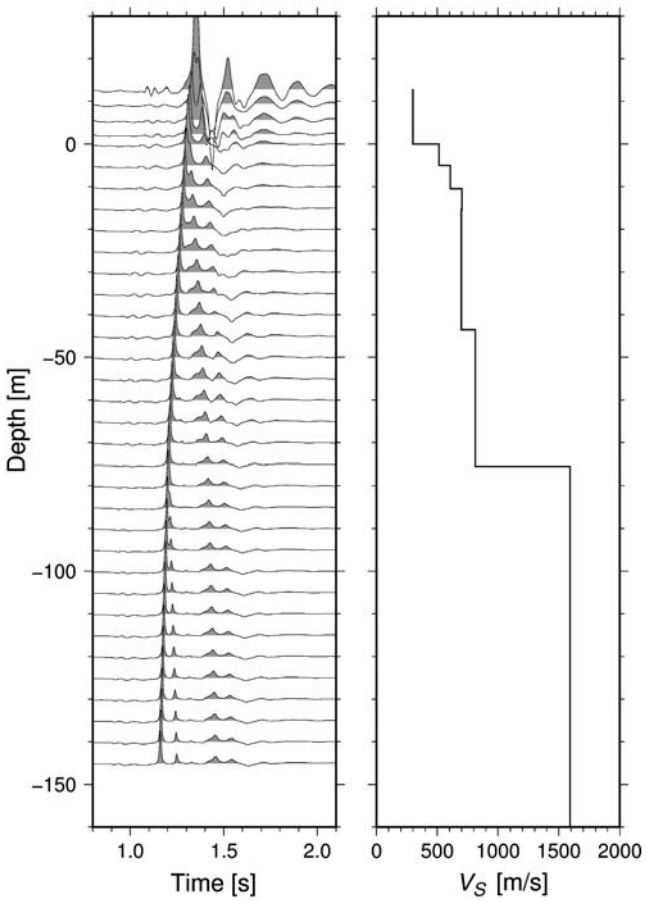

Figure 5. (Left panel) Synthetic seismograms showing the propagation of S waves with nearly vertical incidence between the deepest borehole sensor and the sensor at the top of the building. (Right panel) V_S structure used for the simulation (velocity model V_S for the soil from Parolai *et al.*, 2013, V_S for building layer estimated by the use of the interferometric approach).

is necessary when backprojecting the recordings at the roof to the borehole. In fact, because the recordings at the roof are affected by multireflections within the building, the effect of these multiple reflections (not existing in the acausal part of the signal) must be removed. Hence, for reconstruction of the real input ground motion, both acausal peaks (black lines, equation A4a and A4c) have to be taken into account. The first peak in the causal part of the deconvolved wavefield (black dashed-dotted line, equation A4b) is related to the downward-going wave reflected from the surface, whereas the second one (black-dashed line, equation A4d) is associated with the downward propagation of the wavefield captured within the building (which acts as a soft, i.e., low velocity, layer). This peak (black-dashed line, equation A4d) overlaps with the peak arising from the part of the energy missing in the rooftop recording (the reference) due to the reflection at the Earth's surface (equation A4e), which should be accounted for to correctly reconstruct the borehole recordings when projecting back the recordings on the top. To reconstruct correctly the downward-going wavefield amplitude, we have to separate the contribution of the two different waves to the retrieved wavefield through the consideration of their relative importance directly from the terms $0.5(1 - r)$ (equation A4d) and $r^2/[2(1 + r)]$ (equation A4e) in the Appendix.

When considering the soil layer (and the sensors) below the 75 m discontinuity further, the downward-going wave reflected at the 75-m-deep discontinuity is shown by a dotted black line (Fig. 6). In the case of the synthetic data, the downward-propagating wave can be easily tracked because seismograms were calculated every 5 m. Because in the borehole installation there are only sensors at 85 and 145 m depth, and

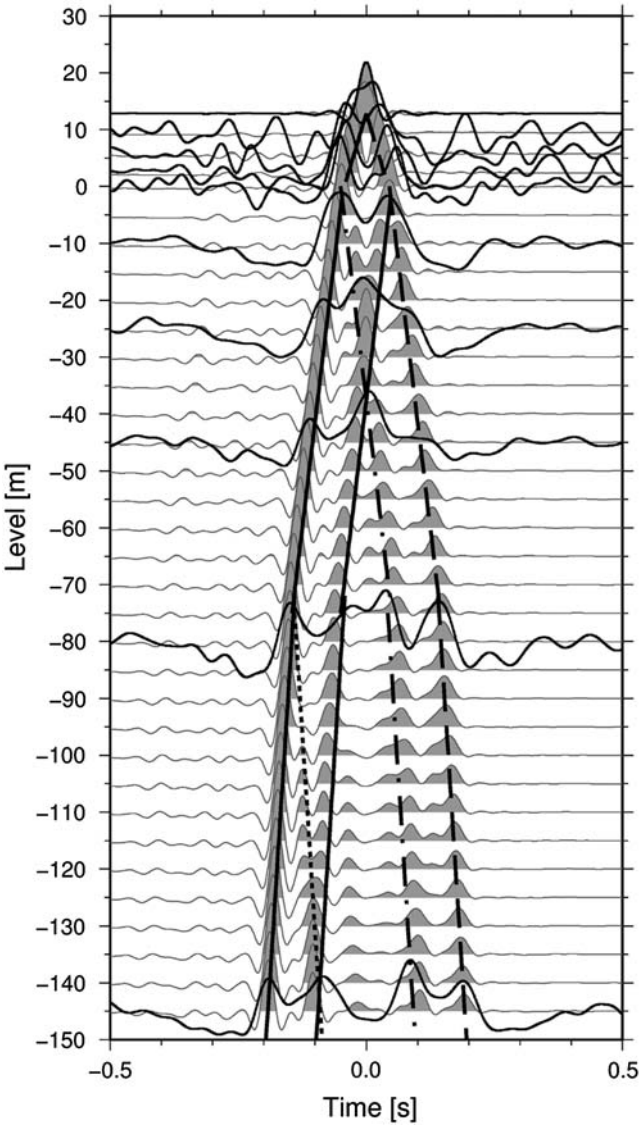

Figure 6. Deconvolved wavefield obtained by the use of synthetic seismograms (gray) and the observed data after stacking the results of all events (black). The upward propagating waves (black lines), the downward-going waves reflected at the interface at 75 m depth (black-dotted line), at the Earth's surface (black dashed-dotted line) and at the top of the building (dashed line) are also shown.

by chance due to the propagation velocities, the second peak in the acausal part (second black line) interferes with the downgoing wave reflected at 75 m depth (dotted black line), these two peaks cannot be separated.

In our case, considering the identified main discontinuity at 75 m depth, the underground structure can be approximated by a layer (from 0 to 75 m) over a half-space with different characteristics. We obtain for the transfer function for the three-layer model, consisting of a building layer, a soil layer from 0 to 75 m, and the half-space (deviation shown in the Appendix) two peaks, one arising from the part of the energy missing in the top roof recording due to the reflection at the discontinuity at 75 m depth (equation A9j), and the other arising from the part of energy missing in the top roof recording due to reflection at the Earth's surface (equation A9i) that are overlying the peak of interest belonging to the downward-going wavefield radiated back from the building (equation A9k; Fig. 6, black-dashed line). To correctly retrieve the amplitude of the wavefield of interest (i.e., the wavefield propagated back into the Earth after propagating through the building), a factor taking into account the relative importance of the contributions of the three waves has to be calculated. Considering also the building, the whole Earth plus building structure can be described by a three-layer model with velocities $v_{\text{building}} = v_b = 300$ m/s, $v_{\text{soil}_1} = v_{s_1} = 870$ m/s, and $v_{\text{soil}_2} = v_{s_2} = 1400$ m/s estimated by the results of deconvolution interferometry. The density of the building layer is computed to be $\rho_b = 400$ kg/m^3, and of the two soil layers as $\rho_{s_1} = 1800$ kg/m^3 and $\rho_{s_2} = 2100$ kg/m^3. Considering these parameters and the terms $r_1^2 r_2/[2(1 + r_1)(1 + r_2)]$ (equation A9i), $[r_2^2(1 - r_1)]/[2(1 + r_2)]$ (equation A9j), and $0.5(1 - r_1)(1 - r_2)$ (equation A9k) in the Appendix, it is estimated that 24% of the wavefield that can be retrieved in the third layer will be due to the wavefield radiated back from the structure.

In the seismic recordings, to quantify the part of the wavefield radiated back from the building to the soil, the real input (i.e., only the incoming waves from the event itself, without the downgoing waves reflected at the interfaces of the soil layers, the Earth's surface, or the top of the building) at the deepest borehole sensor must be isolated first. Then, the portion of the wavefield describing the propagation from the building to the ground needs to be identified by the part of the deconvolved wavefield associated with the downward propagating waves from the building (Fig. 6, black-dashed lines).

Both the real input and wavefield radiated back from the building to the soil is estimated with an approach similar to that proposed by Bindi *et al.* (2010), that is, a constrained regularized scheme (projected Landweber method) is applied (Bertero *et al.*, 1997; Bertero and Boccacci, 1998). For the most appropriate reconstruction of the wavefield radiated back from the building to the soil (in terms of absolute amplitude), as indicated in the previous paragraph, the contribution to the retrieved wavefield should be estimated by considering the main impedance contrasts in the whole building-subsoil structure.

In Bindi *et al.* (2010), the first peak in the acausal part of the deconvolved wavefield alone is associated with the real input ground motion and can be used to reconstruct the input wavefield by convolution with the recordings at the surface. In our case, differently from Bindi *et al.* (2010), as shown in the previous section, the recordings on the top of the building are affected by multiple reflections, and both acausal peaks have to be used to retrieve correctly the real input ground motion. Moreover, as presented already in Parolai *et al.* (2013), part of the energy of the upward-going *S* wave is reflected back at the 75-m-deep discontinuity between the loam and the gravel shingle. The peak of this downward-propagating

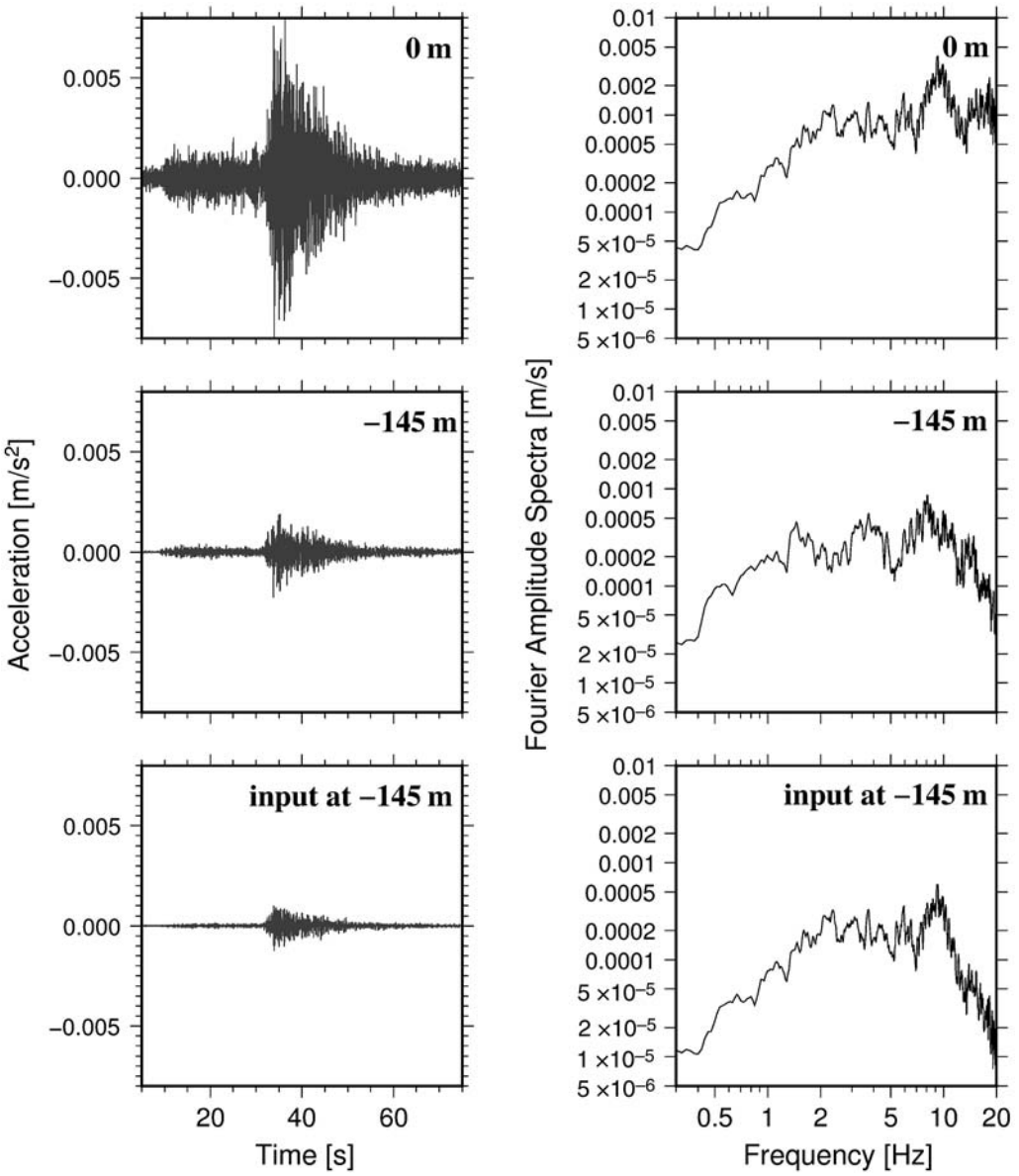

Figure 7. (Left panels) Ground motion recorded at the free surface (top), at 145 m depth (middle), and the reconstructed input motion at 145 m depth (bottom) for event ID 4 (Table 1). (Right panels) Corresponding Fourier spectra of ground motion recorded at the surface (top), 145 m depth (middle), and of retrieved input motion (bottom).

wave reflected at 75 m depth (Fig. 6, black-dotted line) overlaps with the second acausal peak (Fig. 6, second black continuous line) at 145 m depth. Therefore, the free-surface recordings obtained for a station outside of the building structure (sensor at 0 m of the borehole installation) were used as a reference for the interferometric approach (analog as in Bindi *et al.*, 2010), that is, only the borehole sensors are used to retrieve the real input ground motion. The acausal part of the stacked deconvolved borehole wavefield is hence easily extracted and used to reconstruct the input ground motion in the borehole.

Figure 7 (left panels) shows, as an example, the recorded ground motion at the free surface and at 145 m depth, as well as the retrieved real input ground motion at 145 m depth for event ID 4 (Table 1). The corresponding Fourier spectra are shown in the right panels. A clear modification of the recorded spectra at 145 m is visible. In particular, at around 2 Hz, the spectral trough, related to the downward-going waves, disappears.

To obtain the ground motion arising from the wavefield radiated back by the building structure into the soil at each depth, the deconvolution interferometry is performed using the recordings at the top of the building as reference. The downward-going wavefield is reconstructed by the convolution of the recordings at the top of the building and the second peak in the causal part of the deconvolved wavefield using the Bindi *et al.* (2010) approach. In this case, the solution was constrained to be defined in a time interval $t = 0.16$–0.3 s for the recordings at 145 m depth and $t = 0.01$–0.2 s for

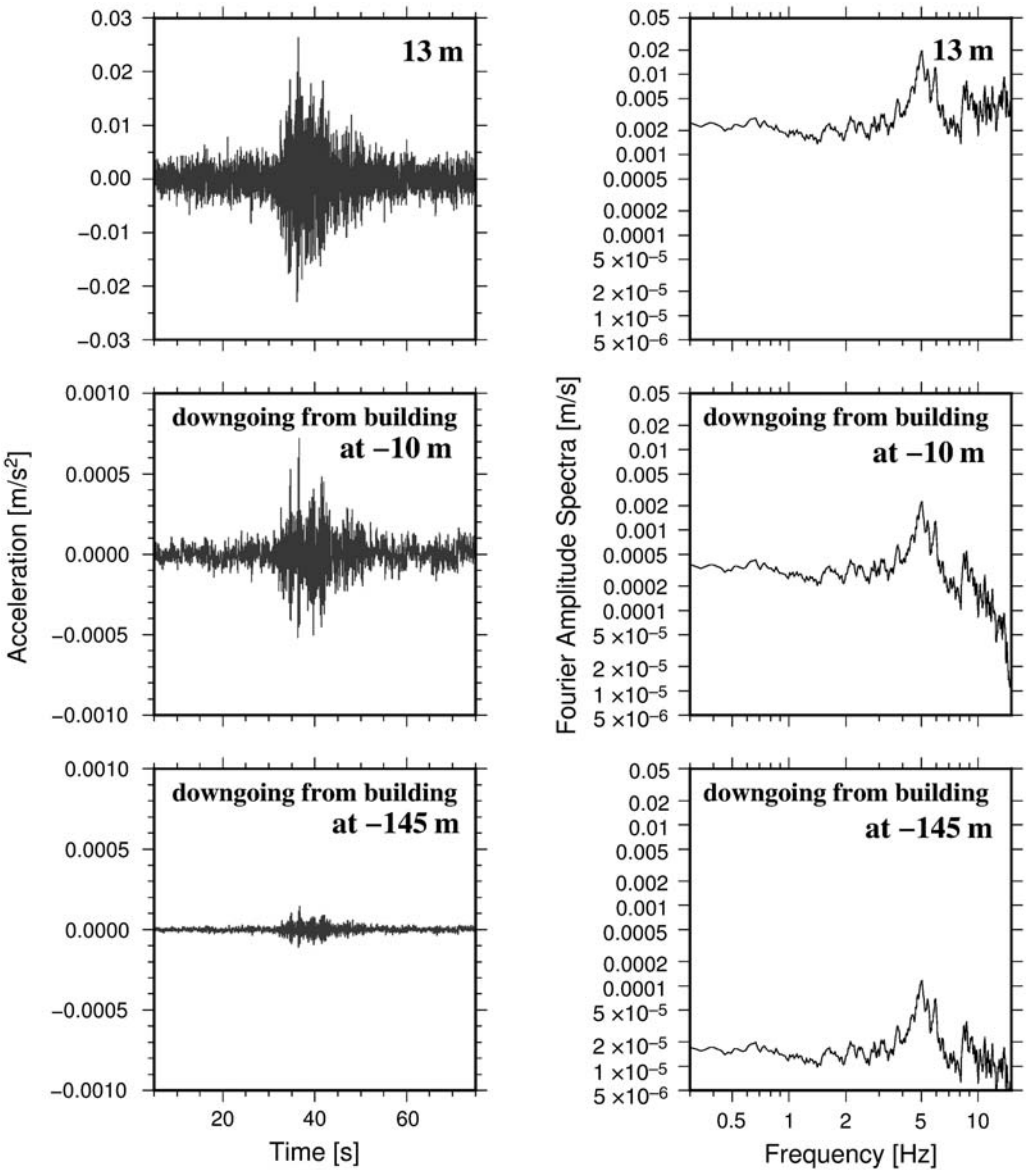

Figure 8. (Left panels) Ground motion recorded at the roof of the building (top), and the retrieved wavefield radiated back from the building at 10 m depth (middle) and at 145 m depth (bottom) for event ID 4 (Table 1). (Right panels) Corresponding Fourier spectra of ground motion recorded at the roof (top), and of the retrieved wavefield radiated back from the building at 10 m depth (middle), and 145 m depth (bottom).

the recordings at 10 m depth. As mentioned before, the amplitude of the wavefield has to be further corrected to consider the appropriate amplitude of the used Green's function.

Figure 8 (left panels) shows, as an example, the recorded ground motion at the top of the building, as well as the retrieved wavefield radiated back from the building at 10 and 145 m depth for the case of event ID 4 in Table 1. The corresponding Fourier spectra are shown in the right panels. Clearly, the energy radiated back from the building is concentrated around 5 Hz and is likely to correspond to the first bending (and dominant) mode in the transverse direction of the structure.

Figure 9 shows the input ground-motion spectra and the spectra of the downward-going waves radiated back from the building to the soil at 10 and 145 m depths for the four analyzed events. In all cases, independent of the spectral shape of the input, a large spectral peak in the downward-going wavefield recording is observed. The amplitude of this peak is clearly diminishing with increasing depth and is smaller than that observed at the top of the building (see for comparison Fig. 8 for event ID 4).

Discussion and Conclusions

In this study, we present the results of an innovative deconvolution wavefield analysis of simultaneous borehole and building recordings. Our results show that it is possible to separate the different components of seismic motion and

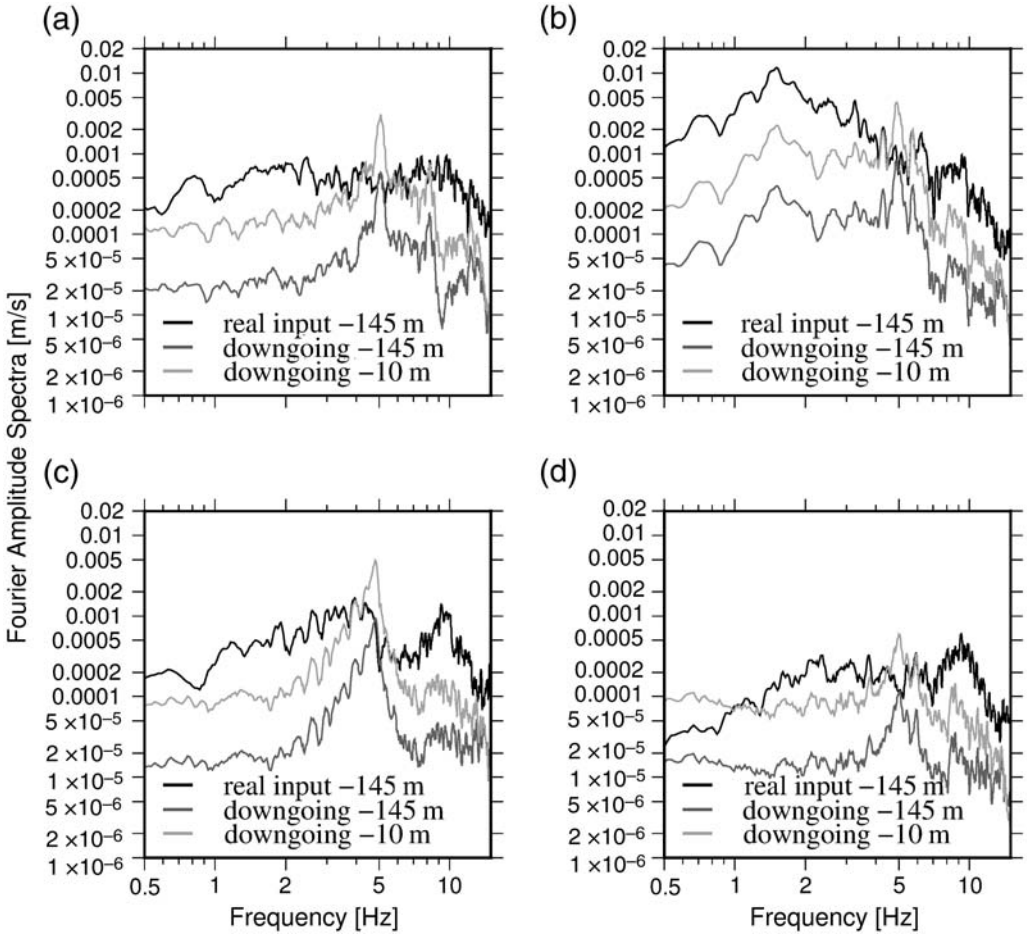

Figure 9. Input spectrum at −145 m (black), spectrum of downgoing waves radiated back from the building at −10 m (light gray), and at −145 m (dark gray) for the four events. (a) M_w 4.9 event (23 November 2013), (b) M_w 5.2 event (14 November 2014), (c) M_w 4.9 event (22 January 2015), and (d) M_w 4.8 event (15 March 2015).

to quantify them. For example, after having integrated the velocity spectra of Figure 9 over the 1–10 Hz frequency band (the same used for the deconvolution), the spectral energy was calculated. The results show that in this case, the energy radiated back by the structure at −145 m corresponds in average to nearly 10% of the energy contained in the real input ground motion within the selected frequency band. When considering the recordings at a 10 m depth, the effect of the wavefield radiated back by the building is larger, leading, on average, to a 40%–50% energy ratio in the selected frequency band.

The potential of the method proposed by Bindi *et al.* (2010) to reconstruct different components of the wavefield (in the linear regime), even for complicated underground velocity structures and without *a priori* knowledge of the velocity and independent knowledge of the quality factor Q of the subsurface, was shown. Only the information about the velocity (which can incidentally be estimated directly by the deconvolution interferometry) and density (mainly of importance for the building structure, but that can be easily estimated) are needed.

These results, although preliminary, highlight, consistent with results of numerical simulations (Bard *et al.*, 1996; Semblat *et al.*, 2004), that the amount of energy radiated back from a structure to the Earth is not negligible and the interactions between nearby buildings are possible. The example considered here is typical for a structure with lower wave velocity than the soil. Analysis of different situations, in which the building structure shows a velocity similar to or lower than the shallow geology layers, is necessary and underway. Furthermore, in this study, only far-source recordings are considered and in the future, when available, the analysis of near-source recordings will be necessary to better understand soil–structure interactions during strong ground shaking. In addition, studying the nonlinear behavior of both building and ground by the analysis of strong-motion recordings might also be an interesting issue for the future. Finally, it is worth mentioning that the influence of the torsional mode of the building onto the deconvolved wavefield is not well studied as of yet; further analyses are needed to understand its influence in detail.

The potential to better understand city–soil interactions, possibly through multiple borehole-building network installations, is obvious and is perhaps one of the main challenges of the engineering-seismology community for the future.

Data and Resources

The seismograms used in this study were collected by downhole accelerometers (located at different levels within a 150-m-deep borehole in the vicinity of the main building of the Central Asia Institute for Applied Geosciences [CAIAG] in Bishkek) and the Self-Organizing Seismic Early Warning Information Network (SOSEWIN) sensors (located at different floors in the CAIAG building, http://lhotse21.gfz-potsdam.de/nagvis/frontend/nagvis-js/index.php?mod=Map&act=view&show=bishkek, last accessed February 2016). These instruments were installed by the German Research Center for Geosciences (GFZ) in cooperation with CAIAG and the data cannot be released to the public.

Acknowledgments

The authors wish to acknowledge Nori Nakata and Norman Sleep for their helpful suggestions to improve this article. We would like to thank A. Strollo, S. Orunbaev, and B. Moldobekov from the Central Asia Institute for Applied Geosciences (CAIAG) who helped with the organization of the Bishkek vertical array (BIVA) planning and installation. Tobias Boxberger, Marco Pilz, and Dino Bindi installed the Self-Organizing Seismic Early Warning Information Network (SOSEWIN) acceleration network in the CAIAG institute. We are grateful to Dino Bindi for the helpful discussions and suggestions to improve our work. Kevin Fleming kindly revised our English. The figures were drawn using Generic Mapping Tool (GMT; Wessel and Smith, 1991).

References

Bard, P.-Y., P. Gueguen, and A. Wirgin (1996). A note on the seismic wavefield radiated from large building structures into soft soils, *11th World Conference on Earthquake Engineering*, Acapulco, Mexico, 23–28 June 1996, Paper no. 1838.

Bertero, M., and P. Boccacci (1998). *Introduction to Inverse Problems in Imaging*, IOP Publishing, Bristol, United Kingdom.

Bertero, M., D. Bindi, P. Boccacci, M. Cattaneo, C. Eva, and V. Lanza (1997). Application of the projected Landweber method to the estimation of the source time function in seismology, *Inverse Probl.* **13,** 465–486.

Bindi, D., T. Boxberger, S. Orunbaev, M. Pilz, J. Stankiewicz, M. Pittore, I. Iervolino, E. Ellguth, and S. Parolai (2015). On-site early-warning system for Bishkek (Kyrgyzstan), *Ann. Geophys.* **58,** no. 1, S0112, doi: 10.4401/ag-6664.

Bindi, D., S. Parolai, M. Picozzi, and A. Ansal (2010). Seismic input motion determined from a surface-downhole pair of sensors: A constrained deconvolution approach, *Bull. Seismol. Soc. Am.* **100,** no. 3, 1375–1380.

Brincker, R., L. Zhang, and P. Andersen (2001). Modal identification of output only systems using frequency domain decomposition, *Smart Mater. Struct.* **10,** 441–445.

Chavez-Garcia, F. J., and M. Cardenas-Soto (2002). The contribution of the built environment to the free-field ground motion in Mexico City, *Soil Dynam. Earthq. Eng.* **22,** 773–780.

Cheng, M. H., M. D. Kohler, and T. H. Heaton (2015). Prediction of wave propagation in buildings using data from a single seismometer, *Bull. Seismol. Soc. Am.* **105,** no. 1, 107–119.

Ditommaso, R., M. Mucciarelli, M. R. Gallipoli, and F. C. Ponzo (2010). Effect of a single vibrating building on free-field ground motion: Numerical and experimental evidences, *Bull. Earthq. Eng.* **8,** 693–703.

Ditommaso, R., S. Parolai, M. Mucciarelli, S. Eggert, M. Sobiesiak, and J. Zschau (2009). Monitoring the response and the back-radiated energy of a building subjected to ambient vibration and impulsive action: The Falkenhof Tower (Potsdam, Germany), *Bull. Earthq. Eng.* **8,** no. 3, 705–722.

Fleming, K., M. Picozzi, C. Milkereit, F. Kühnlenz, B. Lichtblau, J. Fischer, C. Zulfikar, O. Özel, and SAFER and EDIM Working Groups (2009). The Self-organizing Seismic Early Warning Information Network (SOSEWIN), *Seismol. Res. Lett.* **80,** no. 5, 755–771.

Iwan, W. D. (1997). Drift spectrum: Measure if demand for earthquake ground motions, *J. Struct. Eng.* **123,** 367–404.

Kham, M., J.-F. Semblat, P.-Y. Bard, and P. Dangla (2006). Seismic site-city interaction: Main governing phenomena through simplified numerical models, *Bull. Seismol. Soc. Am.* **96,** no. 5, 1934–1951.

Mehta, K., R. Snieder, and V. Grazier (2007a). Extraction of near-surface properties for a lossy layered medium using the propagator matrix, *Geophys. J. Int.* **169,** 271–280.

Mehta, K., R. Snieder, and V. Grazier (2007b). Downhole receiver function: A case study, *Bull. Seismol. Soc. Am.* **97,** 1396–1403.

Nakata, N., and R. Snieder (2014). Monitoring a building using deconvolution interferometry. II: Ambient-vibration analysis, *Bull. Seismol. Soc. Am.* **104,** no. 1, 204–213.

Nakata, N., R. Snieder, S. Kuroda, S. Ito, T. Aizawa, and T. Kunimi (2013). Monitoring a building using deconvolution interferometry. I: Earthquake-data analysis, *Bull. Seismol. Soc. Am.* **103,** no. 3, 1662–1678.

Nakata, N., W. Tanaka, and Y. Oda (2015). Damage detection of a building caused by the 2011 Tohoku-Oki earthquake with seismic interferometry, *Bull. Seismol. Soc. Am.* **105,** no. 5, 2411–2419.

Newton, C., and R. Snieder (2012). Estimating intrinsic attenuation of a building using deconvolution interferometry and time reversal, *Bull. Seismol. Soc. Am.* **102,** no. 5, 2200–2208.

Oth, A., S. Parolai, and D. Bindi (2011). Spectral analysis of K-NET and KiK-net data in Japan, Part I: Database compilation and peculiarities, *Bull. Seismol. Soc. Am.* **101,** no. 2, 652–666.

Parolai, S., A. Ansal, A. Kurtulus, A. Strollo, R. Wang, and J. Zschau (2009). The Ataköy vertical array (Turkey): Insights into seismic wave propagation in the shallow-most crustal layers by waveform, *Geophys. J. Int.* **178,** 1649–1662.

Parolai, S., D. Bindi, A. Ansal, A. Kurtulus, A. Strollo, and J. Zschau (2010). Determination of shallow *S*-wave attenuation by down-hole waveform deconvolution: A case study in Istanbul (Turkey), *Geophys. J. Int.* **181,** no. 2, 1147–1158.

Parolai, S., D. Bindi, S. Ullah, S. Orunbaev, S. Usupaev, B. Moldobekov, and H. Echtler (2013). The Bishkek vertical array (BIVA): Acquiring strong motion data in Kyrgyzstan and first results, *J. Seismol.* **17,** no. 2, 707–719.

Parolai, S., R. Wang, and D. Bindi (2012). Inversion of borehole weak motion records observed in Istanbul (Turkey), *Geophys. J. Int.* **188,** no. 2, 535–548.

Picozzi, M., S. Parolai, M. Mucciarelli, C. Milkereit, D. Bindi, R. Ditommaso, M. Vona, M. R. Gallipoli, and J. Zschau (2009). Interferometric analysis of strong ground motion for structural health monitoring: The example of the L'Aquila, Italy, seismic sequence of 2009, *Bull. Seismol. Soc. Am.* **101,** no. 2, 635–651.

Rahmani, M., and M. I. Todorovska (2013). 1D system identification of buildings during earthquakes by seismic interferometry with waveform inversion of impulse responses—Method and application to Millikan library, *Soil Dynam. Earthq. Eng.* **47,** 157–174.

Safak, E. (1997). Models and methods to characterize site amplification from a pair of records, *Earthq. Spectra* **13,** 97–129.

Semblat, J. F., M. Kham, P. Y. Bard, and P. Gueguen (2004). Could "site-city interaction" modify site effects in urban areas? *13th World Conference on Earthquake Engineering*, Vancouver, British Columbia, Canada, 1–6 August 2004, Paper no. 1978.

Semblat, J. F., M. Kham, P. Gueguen, P. Y. Bard, and A. M. Duval (2002). Site-city interaction through modifications of site effects, *7th U.S. Conference of Earthquake Engineering*, Boston, Massachusetts, 21–25 July 2002.

Snieder, R., and E. Şafak (2006). Extracting the building response using seismic interferometry: Theory and application to the Millikan library in Pasadena, California, *Bull. Seismol. Soc. Am.* **96,** 586–598.

Tikhonov, A. N., and V. Y. Arsenin (1977). *Solution of Ill-Posed Problems*, Wiston/Wiley, Washington, D.C.

Wang, R. (1999). A simple orthonormalization method for stable and efficient computation of Greens functions, *Bull. Seismol. Soc. Am.* **89,** 733–741.

Wessel, P., and W. H. F. Smith (1991). Free software helps map and display data, *Eos Trans. AGU* **72,** no. 41, 445–446.

Appendix

Transfer Function for Two-Layer Model

We are considering a building assumed to be described by the shear-beam model and hence modeled as a layer over a soil layer as schematically shown in Figure A1. We are interested in calculating the transfer function $x(\omega)/y(\omega)$ from the Fourier transforms of $x(t)$ and $y(t)$. The reflection coefficient r for the upgoing waves is defined as

$$r = \frac{\rho_s v_s - \rho_b v_b}{\rho_s v_s + \rho_b v_b} = \frac{c-1}{c+1}, \tag{A1}$$

in which ρ_s and ρ_b are the density of the soil and building layer, respectively. v_s and v_b are the shear-wave velocities in the soil and building layer.

The Fourier transform $x(\omega)$ of $x(t)$ at the soil station can be written as

$$x(\omega) = x_0(\omega) + r x_0(\omega) e^{-i4\pi f \frac{\tau_2}{Q_2}} + 0.5 y(\omega)(1-r) e^{-i4\pi f (\frac{\tau_1}{Q_1} + \frac{\tau_2}{Q_2})}. \tag{A2}$$

$x_0(\omega)$ is the Fourier transform of the incident wave, τ_1 and τ_2 are the travel times for wave propagation from the top of the building to the impedance contrast (building-soil discontinuity), and Q_1 and Q_2 are the quality factors of the building and soil layer, respectively.

The Fourier transform of the recording at the top of the building $y(\omega)$ is given after some mathematical steps as

$$y(\omega) = \frac{2(1+r) x_0(\omega) e^{-i2\pi f (\frac{\tau_1}{Q_1} + \frac{\tau_2}{Q_2})}}{1 + r e^{-i4\pi f \frac{\tau_1}{Q_1}}}. \tag{A3}$$

The transfer function $x(\omega)/y(\omega)$ is finally obtained, analogous to Safak (1997), as

$$\frac{x(\omega)}{y(\omega)} = \frac{1}{2(1+r)} e^{-i2\pi f (-\frac{\tau_1}{Q_1} - \frac{\tau_2}{Q_2})} \tag{A4a}$$

$$+ \frac{r}{2(1+r)} e^{-i2\pi f (\frac{\tau_1}{Q_1} - \frac{\tau_2}{Q_2})} \tag{A4b}$$

$$+ \frac{r}{2(1+r)} e^{-i2\pi f (\frac{\tau_2}{Q_2} - \frac{\tau_1}{Q_1})} \tag{A4c}$$

$$+ 0.5(1-r) e^{-i2\pi f (\frac{\tau_1}{Q_1} + \frac{\tau_2}{Q_2})} \tag{A4d}$$

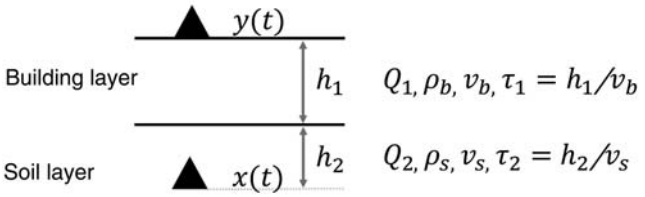

Figure A1. The two-layer model, consisting of the building layer overlying the soil layer (a half-space), with recordings $y(t)$ at the top of the building and recordings $x(t)$ in the soil layer.

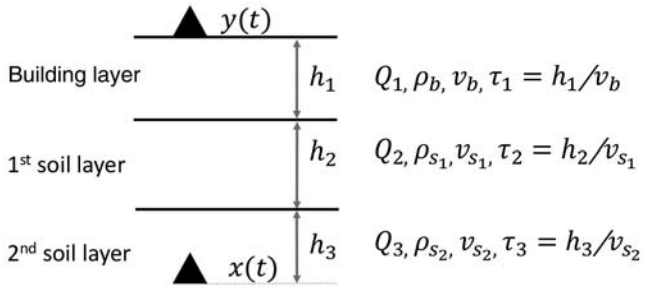

Figure A2. As in Figure A1 but for the three-layer model made up of the building layer over two soil layers (in which the first soil layer is from 0 to −75 m and the second soil layer is a half-space below −75 m) for simplifying the building-subsurface structure in Bishkek.

$$+ \frac{r^2}{2(1+r)} e^{-i2\pi f (\frac{\tau_1}{Q_1} + \frac{\tau_2}{Q_2})}. \tag{A4e}$$

Transfer Function for Three-Layer Model

The layer structure, with the first layer representing the building, is shown in Figure A2. The reflection coefficients r_1 and r_2 at the two impedance contrasts for the upgoing waves are defined as

$$r_1 = \frac{\rho_{s_2} v_{s_2} - \rho_{s_1} v_{s_1}}{\rho_{s_2} v_{s_2} + \rho_{s_1} v_{s_1}} \tag{A5}$$

$$r_2 = \frac{\rho_{s_1} v_{s_1} - \rho_b v_b}{\rho_{s_1} v_{s_1} + \rho_b v_b}, \tag{A6}$$

in which ρ_{s_1} is the density of first soil layer, ρ_{s_2} is the density of second soil layer, ρ_b is the density of building layer, v_{s_1} is the velocity in first soil layer, v_{s_2} is the velocity in second soil layer, and v_b is the velocity in building layer.

The Fourier transform of $x(t)$ (of a sensor installed in the second soil layer) is given as

$$x(\omega) = x_0(\omega) + r_1 x_0(\omega) e^{-i4\pi f \frac{\tau_3}{Q_3}} + \frac{(1+r_1) x_0(\omega) e^{-i2\pi f (\frac{\tau_2}{Q_2} + \frac{\tau_3}{Q_3})}}{1 + r_1 e^{-i4\pi f \frac{\tau_2}{Q_2}}} r_2 (1-r_1) e^{-i2\pi f (\frac{\tau_1}{Q_1} + \frac{\tau_2}{Q_2})} + 0.5 y(\omega)(1-r_1)(1-r_2) e^{-i2\pi f (\frac{\tau_1}{Q_1} + \frac{\tau_2}{Q_2} + \frac{\tau_3}{Q_3})}, \tag{A7}$$

in which τ_1 is the time of wave propagation from top to bottom of the building, τ_2 is the time of wave propagation from top to bottom of first soil layer, τ_3 is the time of wave propagation from discontinuity to sensor at a certain depth in the second soil layer, Q_1 is the quality factor of building layer, Q_2 is the quality factor of first soil layer, and Q_3 is the quality factor of second soil layer.

The Fourier transform of the recording at the top of the building, $y(t)$ can be obtained after some mathematical steps by

$$y(\omega) = \frac{2(1+r_2)(1+r_1)x_0(\omega)e^{-i2\pi f(\frac{\tau_1}{Q_1}+\frac{\tau_2}{Q_2}+\frac{\tau_3}{Q_3})}}{(1+r_1e^{-i4\pi f\frac{\tau_2}{Q_2}})(1+r_2e^{-i4\pi f\frac{\tau_1}{Q_1}})}. \quad \text{(A8)}$$

Finally, the transfer function $x(\omega)/y(\omega)$ can be obtained by

$$\frac{x(\omega)}{y(\omega)} = \frac{1}{2(1+r_1)(1+r_2)}e^{-i2\pi f(-\frac{\tau_1}{Q_1}-\frac{\tau_2}{Q_2}-\frac{\tau_3}{Q_3})} \quad \text{(A9a)}$$

$$+\frac{r_1}{2(1+r_1)(1+r_2)}e^{-i2\pi f(-\frac{\tau_1}{Q_1}+\frac{\tau_2}{Q_2}-\frac{\tau_3}{Q_3})} \quad \text{(A9b)}$$

$$+\frac{r_2}{2(1+r_1)(1+r_2)}e^{-i2\pi f(\frac{\tau_1}{Q_1}-\frac{\tau_2}{Q_2}-\frac{\tau_3}{Q_3})} \quad \text{(A9c)}$$

$$+\frac{r_1r_2}{2(1+r_1)(1+r_2)}e^{-i2\pi f(\frac{\tau_1}{Q_1}+\frac{\tau_2}{Q_2}-\frac{\tau_3}{Q_3})} \quad \text{(A9d)}$$

$$+\frac{r_1}{2(1+r_1)(1+r_2)}e^{-i2\pi f(-\frac{\tau_1}{Q_1}-\frac{\tau_2}{Q_2}+\frac{\tau_3}{Q_3})} \quad \text{(A9e)}$$

$$+\frac{r_1^2}{2(1+r_1)(1+r_2)}e^{-i2\pi f(-\frac{\tau_1}{Q_1}+\frac{\tau_2}{Q_2}+\frac{\tau_3}{Q_3})} \quad \text{(A9f)}$$

$$+\frac{r_1r_2}{2(1+r_1)(1+r_2)}e^{-i2\pi f(\frac{\tau_1}{Q_1}-\frac{\tau_2}{Q_2}+\frac{\tau_3}{Q_3})} \quad \text{(A9g)}$$

$$+\frac{r_2(1-r_1)}{2(1+r_2)}e^{-i2\pi f(-\frac{\tau_1}{Q_1}+\frac{\tau_2}{Q_2}+\frac{\tau_3}{Q_3})} \quad \text{(A9h)}$$

$$+\frac{r_1^2r_2}{2(1+r_1)(1+r_2)}e^{-i2\pi f(\frac{\tau_1}{Q_1}+\frac{\tau_2}{Q_2}+\frac{\tau_3}{Q_3})} \quad \text{(A9i)}$$

$$+\frac{r_2^2(1-r_1)}{2(1+r_2)}e^{-i2\pi f(\frac{\tau_1}{Q_1}+\frac{\tau_2}{Q_2}+\frac{\tau_3}{Q_3})} \quad \text{(A9j)}$$

$$+0.5(1-r_2)(1-r_1)e^{-i2\pi f(\frac{\tau_1}{Q_1}+\frac{\tau_2}{Q_2}+\frac{\tau_3}{Q_3})}. \quad \text{(A9k)}$$

Helmholtz Centre Potsdam
GFZ German Research Centre for Geosciences
Centre for Early Warning
Helmholtzstraße 7
14467 Potsdam, Germany
petrovic@gfz-potsdam.de
petrovic@posteo.de
parolai@gfz-potsdam.de

Manuscript received 23 November 2015;
Published Online 5 July 2016